






















DSP Design for Coherent Optical Point-to-Multipoint Transmission

Thomas Duthel , Christopher R.S. Fludger , Bo Liu , Stenio Ranzini , Antonio Napoli , Nikolai Sölch, Syed M. Bilal , Sofia B. Amado, Saleem Alreesh , Jacqueline Sime , *Member, IEEE*, Amir Rashidinejad , Sezer Erkilinc , Julio Diniz , Aditya Kakkar , Djalal F. Bendimerad , Mathieu Chagnon , Atul Mathur , *Member, IEEE*, Vince Dominic , Parmijit Samra , Henrik Ahlfeldt , Magnus Olson , Han Sun , Azmina Somani, and David F. Welch 

(Invited Paper)

Abstract—A real-time implementation of a coherent optical plug-gable module using digital sub-carrier (DSC) multiplexing has recently been demonstrated. Whilst these modules can support traditional point-to-point (P2P) applications, similar to e.g., 400ZR(+) – with at least the same performance, it is the point-to-multi-point (P2MP) functionality that differentiates their capabilities from a single-carrier implementation. The superior performance of coherent transmission and its insensitivity to link effects, in combination with P2MP capability, allows for new network architectures and can dramatically simplify how metro and access networks are designed. The enabling engine is the DSP ASIC, which generates and demodulates the sub-carriers in the digital domain and furthermore, handles P2MP operation-related aspects. Within the DSP, most of the functional blocks are equivalent to its single-carrier counterpart – even the DSP functionality and algorithms are very similar. Just a few additional mechanisms inside the DSP are needed to process DSCs. This article details the related DSP design and discusses the requirements on the DSP algorithms that accommodate the low per sub-carrier symbol rate and the operation on intermediate digital carriers.

Index Terms—Digital subcarrier (DSC) multiplexing, digital signal processing, point-to-multipoint (P2MP), coherent detection.

Manuscript received 26 June 2023; revised 31 August 2023; accepted 26 September 2023. Date of publication 4 October 2023; date of current version 2 February 2024. (Corresponding author: Thomas Duthel.)

Thomas Duthel, Christopher R.S. Fludger, Bo Liu, Stenio Ranzini, Antonio Napoli, Nikolai Sölch, Syed M. Bilal, Sofia B. Amado, Saleem Alreesh, and Jacqueline Sime are with the Infinera GmbH, 90411 Nuremberg, Germany (e-mail: tduthel@infinera.com; cfludger@infinera.com; boliu@infinera.com; sranzini@infinera.com; anapoli@infinera.com; nsoelch@infinera.com; sbilal@infinera.com; samado@infinera.com; salreesh@infinera.com; jsime@infinera.com).

Amir Rashidinejad, Aditya Kakkar, Han Sun, and Azmina Somani are with the Infinera Corporation USA, Ottawa K2K 2X3, ON, Canada (e-mail: arashidinejad@infinera.com; akakkar@infinera.com; hsun@infinera.com; asomani@infinera.com).

Sezer Erkilinc, Henrik Ahlfeldt, and Magnus Olson are with the Infinera AB, 117 43 Stockholm, Sweden (e-mail: serkilinc@infinera.com; henrik.ahlfeldt@infinera.com; magnus.olson@infinera.com).

Julio Diniz, Djalal F. Bendimerad, Mathieu Chagnon, Atul Mathur, Vince Dominic, Parmijit Samra, and David F. Welch are with the Infinera Corporation, San Jose, CA 95119 USA (e-mail: jdiniz@infinera.com; dbendimerad@infinera.com; mchagnon@infinera.com; amathur@infinera.com; vdominic@infinera.com; psamra@infinera.com; dwelch@infinera.com).

Color versions of one or more figures in this article are available at <https://doi.org/10.1109/JLT.2023.3322076>.

Digital Object Identifier 10.1109/JLT.2023.3322076

I. INTRODUCTION

POINT-TO-MULTI-POINT (P2MP) network architectures based on coherent optical transceivers have the potential to significantly simplify how metro and access networks are designed [1]. Today's P2MP networks – e.g., in the form of passive optical networks (PONs) – are based on intensity-modulated direct detection (IM-DD) transceivers [2]. To support the next generation of wireless network technologies, such as 5 G/6G [3], [4], the backbone optical infrastructure will need to consider some form of coherent technology [5]. First and foremost, this is required to increase the spectral efficiency and throughput, but also to achieve better signal-to-noise-ratio (SNR) and sensitivity performance.

Digital signal processing (DSP) for coherent optical communication systems has traditionally been designed for single-carrier applications, in which the information is directly modulated onto an optical carrier for point-to-point (P2P) transmission. In contrast, digital sub-carrier (DSC) based coherent systems split the information into several narrower, intermediate digital carriers before modulating a comb of these onto the optical carrier [1], [6], [7], [8]. This approach occupies a similar bandwidth as in single-carrier modulation (using the same modulation format and same total transport capacity) and achieves the same spectral efficiency – both per wavelength and over multiple wavelengths in wavelength division multiplexing (WDM) systems. Thanks to the lower per sub-carrier symbol rate, a DSC system provides several advantages: (i) better tolerance to linear and non-linear fiber effects [7]; (ii) support for spectral water-filling [6]; and (iii) enhanced flexibility in capacity assignment [9].

One of the main advantages of a DSC-based coherent system is its P2MP operation capability. In such a configuration, information is exchanged between several geographically distributed leaf nodes and a central hub. Whilst the hub sends and receives all DSCs, the individual leaf nodes only modulate and demodulate a subset of them [1]. Moreover, the network itself can be purely passive, i.e., a passive optical network (PON) with splitters and combiners distributing/aggregating the information without the need for several opto-electronic-opto (O/E/O) conversion layers [10].

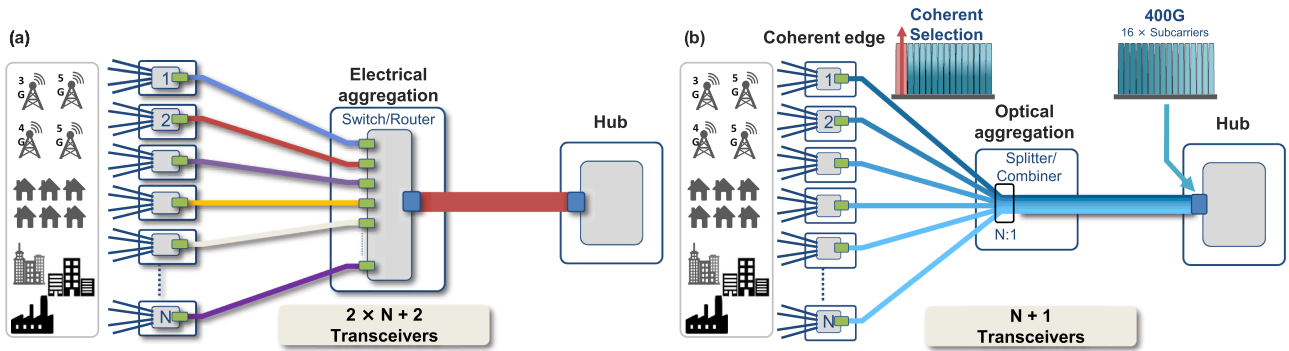


Fig. 1. (a) Point-to-point transceiver-based aggregation network with electrical switch/router; (b) Digital sub-carrier based point-to-multi-point transceiver based aggregation network.

Fig. 1(a) depicts how a P2MP network at the edge of the core might look today and how it can be simplified with DSC-based transceivers (Fig. 1(b)). Despite the significant reduction of the number of incorporated transceivers ($2 \times N + 2$ to $N + 1$, where N is the number of low-speed transceivers drawn as green boxes in Fig. 1), there is also the simplification of the O/E/O aggregation site which can be replaced by passive optical splitters/combiners. In such a network design, capacity upgrades may be handled without further hardware deployment, e.g., via a software reconfiguration of the transceivers, simply by assigning more DSCs to a particular leaf location and/or by upgrading only the nodes that exceeded their capacity limit. This feature enables clustering traffic over time, and thus, reduces capital (CAPEX) and operational expenditure (OPEX) [11].

To minimize CAPEX, different flavors of a DSC-based DSP can be used to suit different functions inside a P2MP network. A hub transceiver and its DSP would be designed for a large number of DSCs, whilst a leaf node transceiver would need to be more power efficient with a fewer number of DSCs, allowing for smaller form factors, e.g., QSFP-28 and lower cost modules. This solution has the advantage to match typical traffic patterns in metro-aggregation networks, where a multitude of antennas, business buildings or campuses, will generate different flows (from leaf nodes) and transmit them to a central office or a data center (hub node). A careful decision on a base set of features (e.g., DSC symbol rate, modulation format, and forward error correction (FEC) coding scheme) allows for a multi-generation design that benefits from power savings over application-specific integrated circuit (ASIC) node sizes while maintaining compatibility with earlier generations. Furthermore, the dynamic and flexible capacity upgrade capability helps to reduce electronic waste since device upgrades are only needed when capacity limits are reached [1], [12].

In this article, we describe the architecture of a DSC-based DSP supporting P2MP operation. The remainder of the article is structured as follows: In Section II, we report a detailed description of the DSC-based transceiver module (including the DSP building blocks) and compare it against a single-carrier implementation. In Section III, we describe the special aspects of a DSC and P2MP-based operation supported with measurements using a real-time coherent P2MP transceiver. In Section IV, we report on a further experiment with a 400 G hub node and four

100 G leaf nodes. Leaf nodes are added and dropped whilst existing transmission data is preserved. The last Section V draws the conclusions.

II. DSP BUILDING BLOCKS

A coherent DSP for DSCs incorporates various of the same functional blocks as a single-carrier DSP. The main difference is that most functional blocks are instantiated as one large circuit in single-carrier and multiple smaller circuits in DSC systems. It is worth pointing out that, although the total symbol rate may be in the 50 to 100 GBaud region, the core clock rate for an ASIC is typically ~ 1 GHz such that all algorithms, whether single-carrier or DSC-based, will be implemented in a highly parallel manner.

Fig. 2 shows a side-by-side comparison of the two transceiver types. In both architectures, the transmitter applies FEC encoding and framing followed by a pulse shaping (here root-raised-cosine (RRC)) filter, which usually also performs pre-compensation of, e.g., analog bandwidth restrictions and timing skews. In the single-carrier architecture, the output of the pulse shaping filter is converted to an analog signal by a set of four digital-to-analog converters (DAC) and finally modulated onto the optical carrier by a dual-polarization optical IQ Mach-Zehnder modulator fed by a narrow linewidth laser. For digital sub-carrier processing, there is only one additional processing block strictly required. It sits in front of the DAC and digitally modulates (muxes) the individual baseband sub-streams onto intermediate subcarriers (DSC Mux). The gain control blocks (Gain cntrl) per DSC shown in the block diagram may be used to control the relative DSC power to counteract e.g. link losses.

The RX processing starts with a standard coherent detector using a narrow linewidth local-oscillator laser, a 90° hybrid, and a set of balanced photodetectors for both architectures. After sampling by a four-channel analog-to-digital converter (ADC), the signals are fed into the RX DSP before the FEC decoder applies error correction.

The RX DSP itself counteracts link chromatic dispersion (CD), and compensates, e.g., analog bandwidth restrictions and timing skew, polarization de-muxing (POL), carrier and frequency recovery (CR). Whilst these steps are performed on the full bandwidth of a single-carrier signal, a sub-carrier DSP

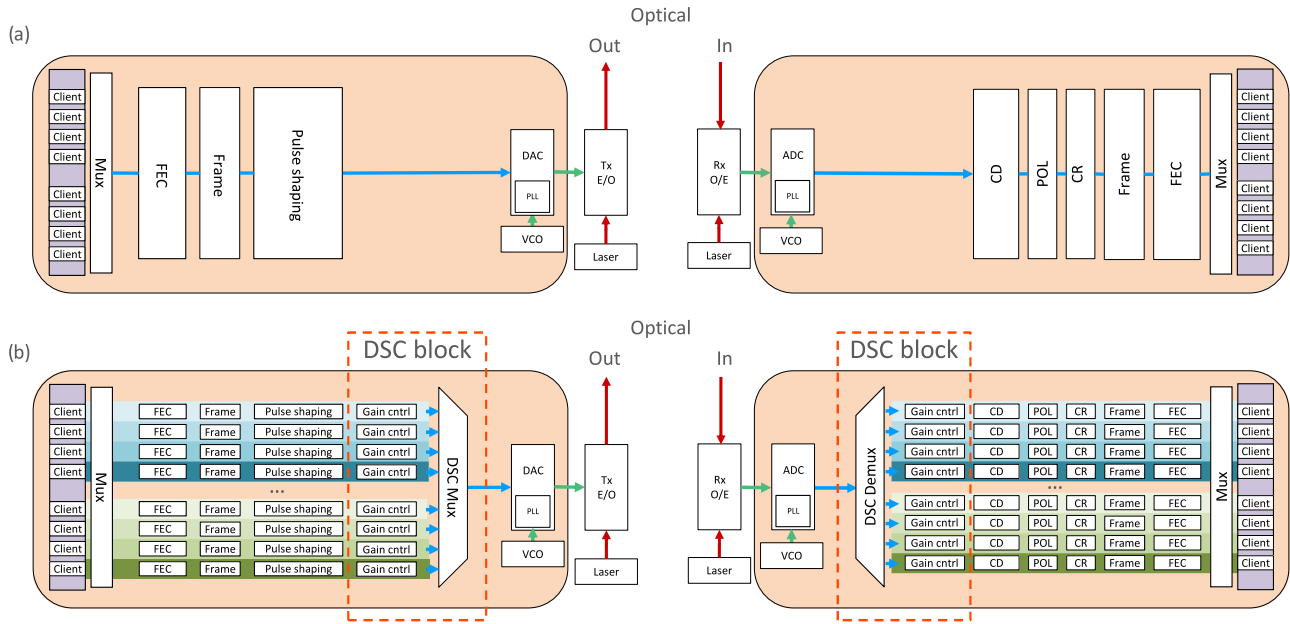


Fig. 2. (a) Single channel transceiver schematic; (b) Digital sub-carrier transceiver schematic.

first de-multiplexes individual sub-streams to near baseband (DSC Demux) before independent modems can apply the signal processing steps described above. As on the TX side, gain control blocks may help to counteract gain imbalances between sub-carriers.

III. SPECIAL ASPECTS OF DIGITAL SUB-CARRIERS AND POINT-TO-MULTIPOINT OPERATION

Despite the mux/demux and the DSC gain control block, there are minimal differences in the optical, analog, and digital implementation of a sub-carrier system. Even the DSP [13] and FEC algorithms can be very similar to a single-carrier implementation. Differences in requirements, complexity, and implementation are related to the low sub-carrier symbol rate and the operation on intermediate digital frequencies. Additionally, there are P2MP operation-related aspects that require special mechanisms and treatment, which represent the foundations of the benefits enabled by this proposed technology. Nevertheless, since almost all processing steps in the sub-carrier architecture take place on a per DSC basis, mitigating linear link impairments (e.g., CD, differential group delay (DGD), filtering) is straightforward, even if the different DSCs propagate along different links.

A. Timing Recovery

Inaccuracies in reference timing oscillators from each leaf node result in slight differences between DSCs which are all sampled by a common ADC. Due to the low tuning bandwidths of the reference oscillators, and the latency in the DSP calculation, digital clock recovery is often used in single-carrier coherent receivers [14], [15]. This allows robust timing phase information to be extracted after removing channel distortion (e.g., CD). Digital interpolation can then be applied to avoid

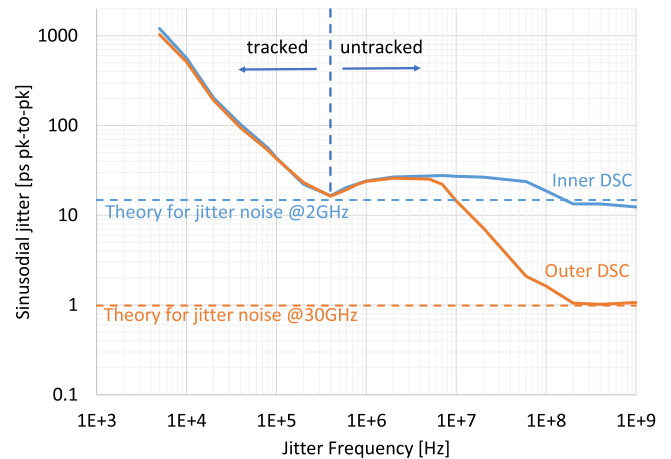


Fig. 3. Impact of sinusoidal jitter on 16QAM for 0.5 dB Q-factor penalty at 14 dB SNR.

long feedback paths to the reference oscillator such that the loop bandwidth can be kept high. An identical strategy can be applied for DSC-based receivers where smaller separate timing recovery circuits are applied to each DSC.

An interesting difference between single-carrier and DSC-based systems can be observed in the closed-loop tolerance to timing jitter shown in Fig. 3. In this Monte-Carlo simulation for a 16 DSC 16QAM sub-carriers system at ~ 4 GBaud, the timing recovery is closed with a 3 dB loop bandwidth of 250 kHz and then perturbed with sinusoidal jitter at different frequencies and amplitudes.

Within the tracked region (defined by the loop bandwidth), the performance of inner and outer DSCs remains the same, whilst at high frequencies, outer DSCs (here at ~ 30 GHz) have less tolerance than inner DSCs (here at ~ 2 GHz). For a SNR

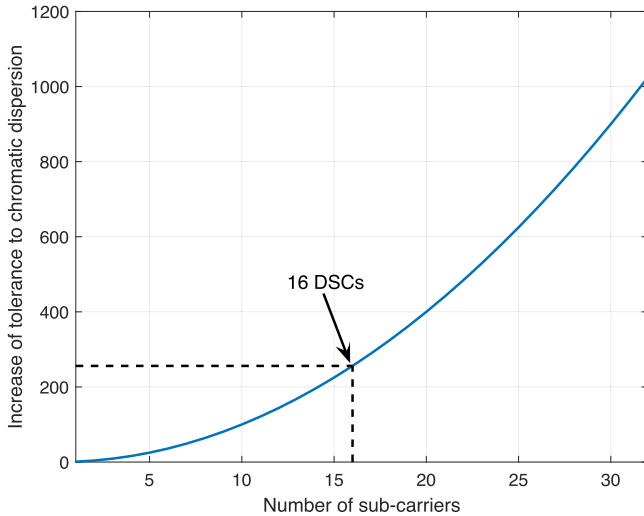


Fig. 4. Increase of tolerance to chromatic dispersion for a fixed number of CD filter coefficients.

degradation of 0.5 dB from a reference SNR of 14 dB, the SNR from the clock jitter would be 23.6 dB, and the clock noise σ_{clk} can be found at a given frequency f_c according to [16]:

$$SNR_{clk_dB} = -20 \log_{10}(2\pi f_c \sigma_{clk}) \quad (1)$$

The theoretical peak-to-peak jitter is, therefore:

$$J_{pk-pk} = 2\sqrt{2}\sigma_{clk} = \frac{2\sqrt{2}}{2\pi f_c} 10^{\frac{-SNR_{clk_dB}}{20}} \quad (2)$$

Although the absolute jitter requirements are well within the capability of modern phase-locked loop (PLL) design, the high-frequency clock noise requirement for inner DSCs is over $10\times$ more relaxed than for the outer DSCs.

Note that DSCs received from different leaf node transmitters run on their own clock reference. This leads to timing errors and difference jitter between DSCs received on a hub. Although the per DSC clock recovery circuits can retune the signal, a closed-loop feedback like the one described for the carrier recovery in Section III-C might be desirable.

B. Chromatic Dispersion and PMD Compensation

The receiver DSP tolerance to linear link impairments such as CD and polarization mode dispersion (PMD) is symbol rate dependent since the associated channel memory scales with the signal bandwidth. Whilst the memory of first-order PMD (i.e. DGD) scales linearly, the CD memory scales quadratically [17]. This directly affects the size and design of the receiver-side digital filters [18]. In sub-carrier systems, each sub-carrier spans a fraction of the bandwidth of a single-carrier system. Due to the quadratic relationship between tolerable CD and channel bandwidth, DSCs can tolerate much more CD for a given filter impulse response (see Fig. 4), e.g., a 16 sub-carrier system has $256\times$ the dispersion tolerance of a single-carrier system.

Therefore, a sub-carrier system needs less complexity in the bulk CD filter for a given amount of tolerable CD. It is

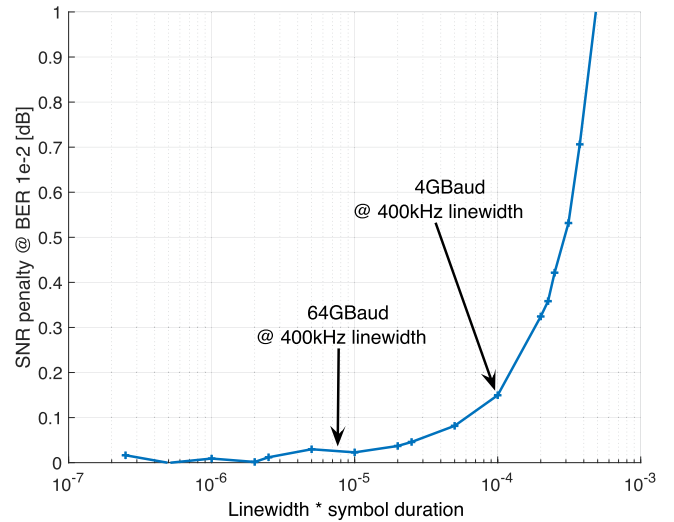


Fig. 5. Simulated 16QAM SNR penalty depending on linewidth symbol-duration product.

worth noting that the sub-band filter approach for single-carrier systems [19] makes use of the same scaling effect, but discontinuities between filter sub-bands cause performance penalties. This is not the case for sub-carrier systems since the sub-band is chosen to match the width of a sub-carrier.

C. Carrier Recovery

Recovering the carrier is one of the few operations that becomes simpler as the symbol rate increases. The reason is the following: the laser phase noise causing the phase variation is independent of the symbol rate, and higher symbol rates allow for a finer resolution of the phase variation in time [20]. In fact, the higher symbol rate of 400ZR (64 GBaud) allows low-complexity implementations where phase estimates are only performed on known pilot symbols spaced every 32 symbols [21].

Fig. 5 shows the impact of Gaussian laser phase noise (linewidth) on the system performance of a blind phase search carrier recovery scheme [22]. It can clearly be seen that a high symbol rate system with its shorter symbol duration suffers less penalty from the same linewidth than a sub-carrier with a multiple of the symbol duration. In the example given in the figure, a 16×4 GBaud sub-carrier system suffers a moderate SNR penalty (<0.2 dB at BER 10^{-2}) compared to a single-carrier system.

Therefore, choosing a suitable carrier recovery scheme is crucial to guarantee system performance for sub-carriers, and depending on the actual sub-carrier symbol rate, well-known recovery schemes [23] might not be the best choice.

A second effect related to laser phase noise that, in this case, favors lower symbol rates is the equalizer-enhanced phase noise (EPPN). This effect describes the interplay between local oscillator phase noise and the RX bulk CD filter. High amounts of compensated CD change the nature of the phase noise (phase to amplitude conversion) and prevent a proper compensation of the LO phase noise contribution in the carrier phase recovery [24]. Since the effect of EPPN decreases when lowering the symbol

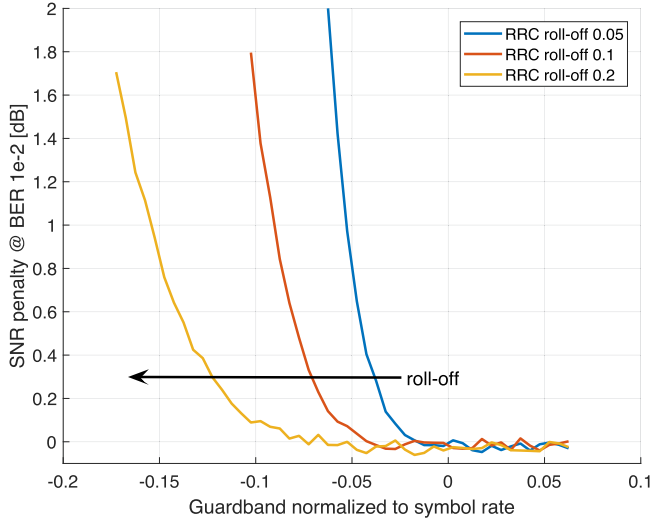


Fig. 6. Simulated SNR impact of guard bands between adjacent 16QAM DSCs.

rate, it has a smaller impact in a sub-carrier system [6], compared to a single-carrier one.

D. Laser Frequency Clock Control

In a single-carrier system, the achievable spectral efficiency depends on the TX side shaping (usually the roll-off of the RRC pulse shaping) and the stability of the TX lasers. Without additional means of stabilization, adjacent wavelength channels must be spaced with guard bands of several GHz to prevent collisions.

The same fundamental mechanisms apply in sub-carrier systems, but the P2MP operation requires additional restrictions, as sub-carriers arriving at the hub (from different leaf transmitters) may run on their own wavelength references (wavelength lockers). Those references are no more precise than those used in single-carrier and typically guarantee absolute accuracies of ± 1.5 GHz. This is not enough to prevent collision/overlap between adjacent sub-carriers coming from different leaf nodes.

The impact of laser frequency variation on the SNR performance can be reduced by increasing the spectral distance Δf_{DSC} between adjacent sub-carriers via a guard band (GB), which reads as

$$\Delta f_{DSC} = BR(1 + RO) + GB \quad (3)$$

where BR is the sub-carrier symbol rate and RO is the RRC roll-off. Whilst GBs < 0 Hz lead to performance penalties (depending on RRC roll-offs), any guard bandwidth > 0 Hz allows for penalty-free operation (see Fig. 6). However, to keep the spectral efficiency high and the required electrical and optical bandwidth low, the guard bands need to be kept as small as possible.

Small GBs can be accomplished with standard lasers by locking the leaf laser wavelength/frequency to that of the remote hub. This is possible in systems with shared TX/RX lasers (as shown in Fig. 7), where the frequency estimate from the leaf's

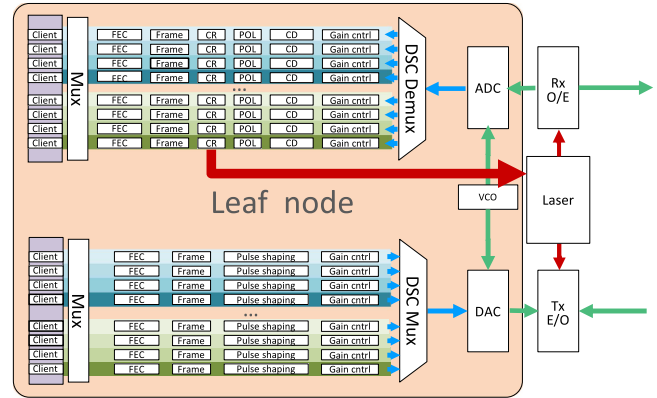


Fig. 7. Leaf node laser frequency control scheme.

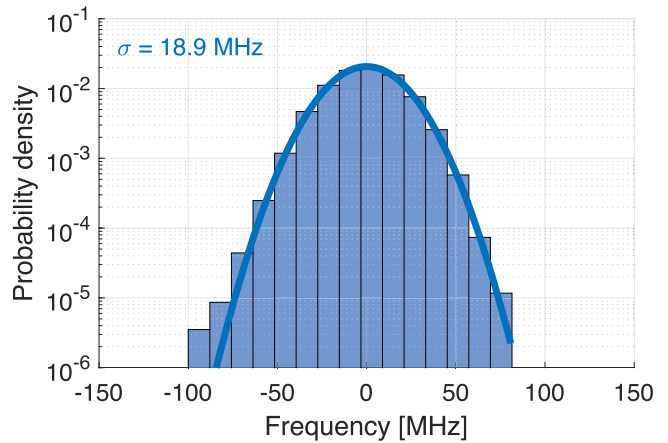


Fig. 8. Measured joint frequency variation histogram for leaf node and hub side laser.

CR can be used to control the laser frequency of the leaf side laser (feeding TX and RX optics). In this way, the leaf and hub lasers are coarsely frequency locked. This approach works for all leaf nodes connected to a hub since the frequency control happens on the leaf side, whilst the hub laser runs on its own reference. As the hub laser frequency drifts due to aging or temperature, all leaf nodes automatically adjust their laser frequencies.

Fig. 8 shows the laser frequency variation measured between a leaf and a hub in a closed-loop real-time DSC P2MP system. The frequency variation was recorded from the hub-side carrier recovery. A Gaussian distribution well represents the observed behavior, and the joint standard deviation of both lasers is below 20 MHz. Based on this standard deviation, the minimum required GB between adjacent sub-carriers to support 20 years of collision-free operation is ~ 235 MHz [25].

E. TX and RX Impairments

IQ (timing) skew, quadrature error, IQ (power) imbalances, and IQ (DC) offset are metrics to quantify distortions caused inside the electrical and optical processing chain. These impairments are not necessarily associated with a particular physical location (e.g., IQ skew can be caused in the analog and/or optical

TABLE I
EFFECT OF TX SIDE IMPAIRMENTS FOR SINGLE-CARRIER AND SUB-CARRIER SYSTEMS

Impairment	Single-carrier (carrier centered)	Sub-carrier (carrier off-center)
Quadrature error	Trapezoid constellation	Mirror frequency image
IQ gain imbalance	Rectangular constellation	Mirror frequency image
IQ offset	Constellation shifted away from origin	No impact
IQ skew	Widened constellation points	Mirror frequency image (growth with sub-carrier frequency)

domain) and their impact might be slightly different on receiver side due to LO to signal frequency offset, but these metrics can be seen as general indicators for the signal quality. This is true for both, single-carrier and sub-carrier systems, but the effect on the signal differs for the two cases (Table I compares how impairments affect single-carrier and sub-carrier transmitters).

For single-carrier transmitters, most impairments are easily seen in the constellation diagram [26]. Indeed, test equipment manufacturers use measurements inside the constellation diagram to quantify these impairments. The clear association between constellation properties and impairment is possible since impairments impact the single-carrier signal “on the axis”, e.g., IQ imbalances directly shorten/elongate the in-phase and/or quadrature component, which leads to a rectangular rather than quadratic constellation diagram.

In contrast, for DSC systems, the complex-valued baseband signal \underline{x}_{DSC} is modulated onto an intermediate carrier with angular carrier frequency ω_{DSC}

$$x_I(t) + i \cdot x_Q(t) = \underline{x}_{DSC}(t) \cdot e^{i\omega_{DSC}t} \quad (4)$$

The drive signals into the optical IQ modulator, in this case, are represented by x_I and x_Q with

$$x_I(t) = \Re\{\underline{x}_{DSC}(t)\} \cdot \cos(\omega_{DSC}t) - \Im\{\underline{x}_{DSC}(t)\} \cdot \sin(\omega_{DSC}t) \quad (5)$$

$$x_Q(t) = \Im\{\underline{x}_{DSC}(t)\} \cdot \cos(\omega_{DSC}t) + \Re\{\underline{x}_{DSC}(t)\} \cdot \sin(\omega_{DSC}t) \quad (6)$$

Adding electrical and/or optical IQ impairments yields

$$\begin{aligned} \underline{x}_{opt}(t) = & \sqrt{1 - \frac{IB-1}{IB+1}} x_I \left(t - \frac{\tau}{2} \right) e^{-i\frac{\theta}{2}} \\ & + i \sqrt{1 + \frac{IB-1}{IB+1}} x_Q \left(t + \frac{\tau}{2} \right) e^{+i\frac{\theta}{2}} \end{aligned} \quad (7)$$

where \underline{x}_{opt} is the output of the optical IQ modulator, IB is the (linear) IQ imbalance ($IB[dB] = 10 \cdot \log_{10}(IB)$), τ is the IQ skew, and θ is the quadrature error.

Due to the modulation onto an intermediate carrier, the constellation is already rotating when it hits the impairments, and distortions to the constellation are almost imperceptible. Instead, energy is transferred from the generated sub-carrier

into its mirror position on the other side of the spectrum (see Appendix A for the analytical derivation). This energy transfer does not immediately affect the performance of the sub-carrier itself but generates a crosstalk component that affects a sub-carrier located at the frequency of the mirror image position (and vice versa). Note this behavior is similar for transmitter and receiver, although the LO to signal frequency offset needs to be taken into account on receiver side.

Fig. 9 exemplarily depicts the described behavior for TX side IQ skew. The measurements are taken on a real-time DSC P2MP transceiver, which supports up to 16×4 GBaud 16QAM dual polarization DSCs, each transmitting 25 Gbit/s of data.

The two top insets show the measured spectrum without (Fig. 9(a)) and with ~ 3 ps of TX IQ skew (Fig. 9(b)), whilst the eight right-hand side DSCs are turned off. In both cases, all active DSCs show undistorted 16QAM constellation diagrams. The only noticeable difference is the mirror images caused by IQ skew on the other side of the frequency spectrum in Fig. 9(b). The strength of the images depends on the IQ skew value and increases with frequency offset. The impact from the IQ skew distortion is important when the whole spectrum is filled with DSCs, e.g., in the case a hub sends towards a leaf node. Here, all DSCs are turned on, and the mirror image from the left-hand side DSCs distorts the right-hand side DSCs and vice-versa. This is shown in Fig. 9(c). Due to the residual/uncompensated IQ skew, DSCs are more distorted the further they are away from the center of the spectrum. It is worth noting that the ~ 3 ps introduced is significant for systems with a total symbol rate of 64 GBaud [26], as simulated in Fig. 10 for single-carrier (green curve) and 16 DSC 16QAM (blue curves). As inferred from the spectra and constellation diagrams shown in Fig. 9, the penalty associated with TX IQ skew strongly depends on the position within the signal bandwidth [27]. Whilst inner sub-carriers (close to optical carrier) are almost insensitive to IQ skew, outer sub-carriers suffer, and the most outer ones in a 64 Gbaud system can only tolerate ~ 0.4 ps for 0.25 dB SNR penalty at pre-FEC BER 10^{-2} . In comparison, a single-carrier system operated at the same total symbol rate can tolerate almost twice the IQ skew at the same penalty, as the distortion due to the mirror image is averaged out over the entire signal bandwidth.

Likewise, as for single-carrier transceivers, it can be seen that TX and RX side impairments need to be calibrated during manufacturing, and it is highly desirable to minimize or compensate their impact over lifetime and operating conditions [26], [28].

F. Digital Sub-Carrier Power Control

The digital sub-carrier power control mechanisms on the transmitter and the receiver side, shown in Fig. 2(b), fulfill slightly different purposes.

The TX side mechanism can adapt the power of (groups of) sub-carriers. Since the mechanism is implemented in the digital domain, its dynamic range is limited by the quantization inside the DSP and the full-scale range of the DAC. Besides optimization of the digital drive into the DAC for different numbers of sub-carriers, the mechanism can also be used to

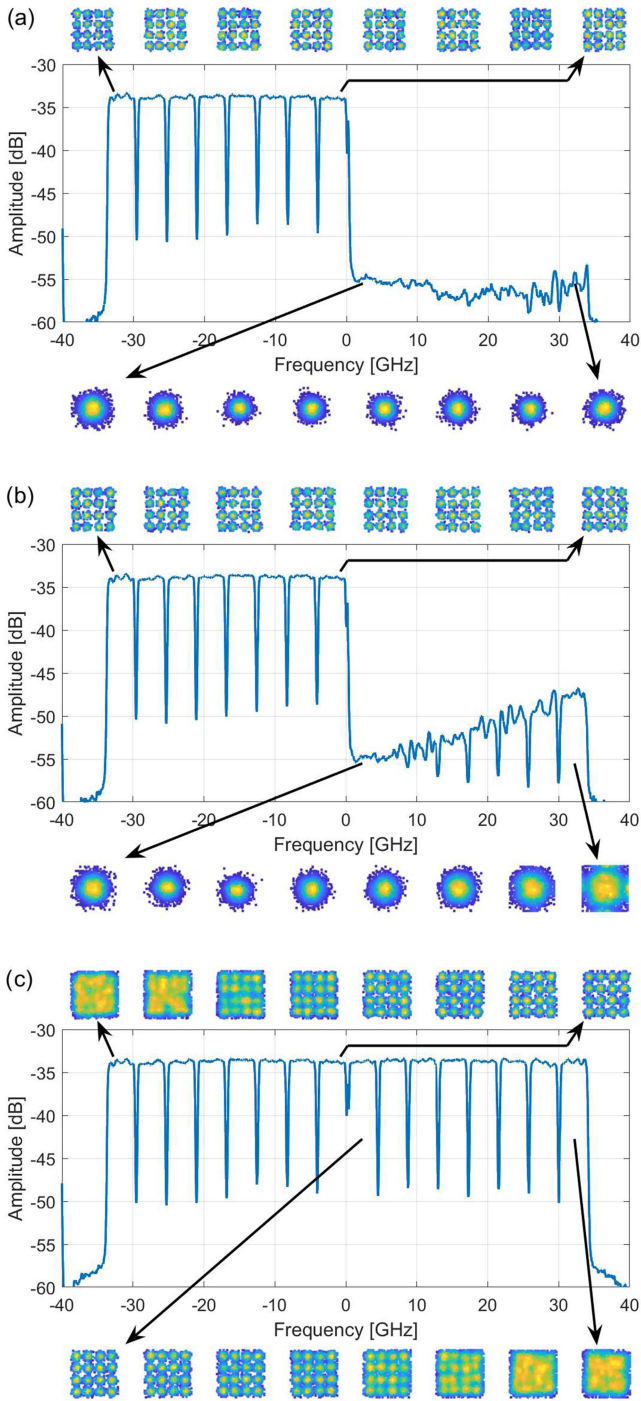


Fig. 9. Measured impact of TX side residual IQ skew: (a) single sideband without IQ skew; (b) single sideband with ~ 3 ps IQ skew; (c) double sideband with ~ 3 ps IQ skew.

equalize the RX side SNR between sub-carriers experiencing different noise loading.

The RX side control, in contrast, cannot improve the link SNR nor the SNR contribution from the RX side front-end. In the best case, it can optimize the quantization noise contribution inside the RX DSP. Its main purpose is reducing the dynamic range requirements of the adaptive digital filter – also under transient conditions.

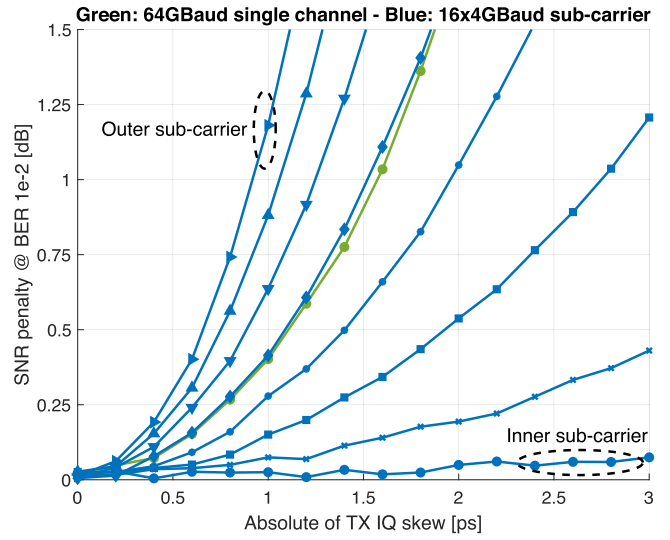


Fig. 10. Simulated impact of TX IQ skew on 16QAM (RRC roll-off 0.05). Only DSCs right hand of the optical carrier are shown; left-hand DSCs behave the same.

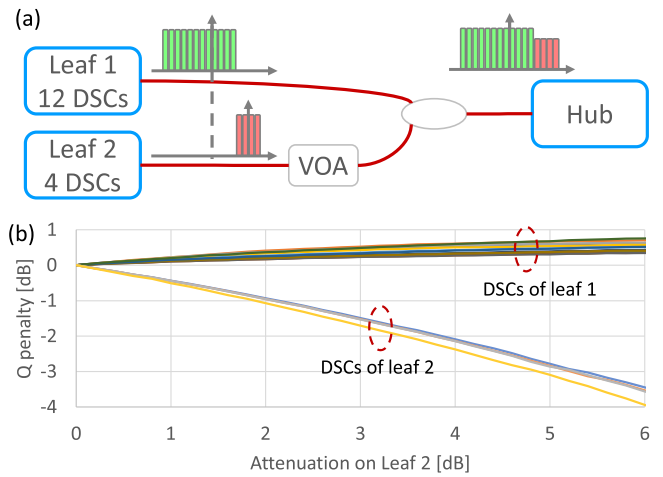


Fig. 11. Tolerance to power imbalances between sub-carriers (a) Setup; (b) Measured Q penalty vs. attenuation on leaf 2.

Fig. 11(a) shows a simplified experimental P2MP system with two leaf nodes connected to a hub site. Leaf 1 generates 12 DSCs on the left-hand side of the spectrum, and leaf 2 adds another 4 DSCs to the right-hand side. All 16 DSCs are received by a single hub. Different link losses between leaf nodes and hub are mimicked by a VOA placed at the output of leaf node 2 (the power of the DSCs coming from leaf 1 is kept constant).

Fig. 11(b) shows the impact of static attenuation at the output of leaf 2. The Q factor of the DSCs coming from leaf 1 show a performance improvement as the 4 DSCs from leaf 2 get attenuated. This is due to the slight changes in the RX noise contribution with reduced power from leaf 2. For leaf 2 itself, the situation is different, and an attenuation from the VOA results in a Q penalty degradation which is caused by the RX side noise. However, it is worth noting that the gain control mechanism inside the RX DSP allows demodulation of DSCs from leaf 2

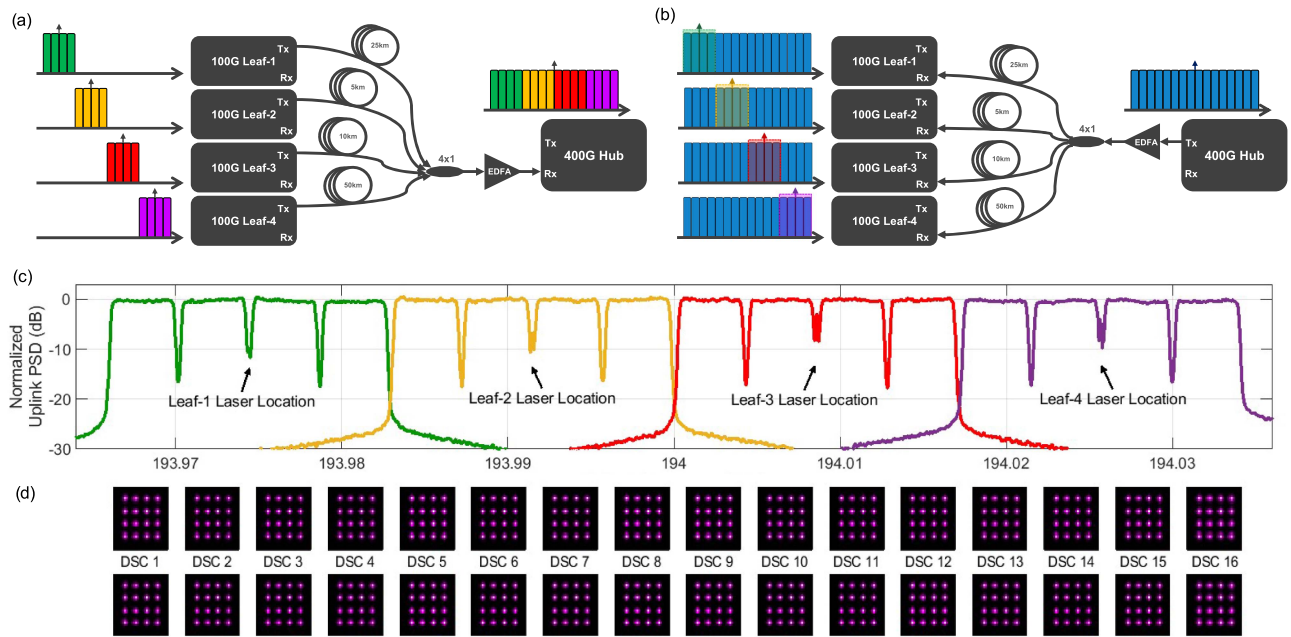


Fig. 12. 4×100 G leaf node to hub experiment, (a) upstream direction; (b) downstream direction; (c) received spectrum at the hub; (d) constellation diagrams (X- and Y-pol separated) received at the hub.

even if their power was several dB below the DSCs coming from leaf 1. In real network scenarios, the situation could be further improved by instructing the leaf 2 TX to increase its power, e.g., using the TX side gain control mechanism. Such operation requires a feedback channel from the hub to the leaf.

IV. POINT-TO-MULTI-POINT EXPERIMENTS

Fig. 12 depicts a P2MP network scenario typically found at the edge of the core network [29]. The investigated system is built based on real-time transceivers supporting 16 DSC dual-polarization 16QAM operation. In the experiment four leaf modules simultaneously send and receive data to and from a hub node. It is worth noting that the leaf nodes are at different distances from the hub location (25 km, 5 km, 10 km, and 50 km), and signals experience different fiber losses and impairments (e.g., CD). To compensate for fiber propagation and coupler losses, an erbium doped fiber amplifier (EDFA) is placed at the hub RX side to pre-amplify the signals coming from the leaf nodes (upstream), while another EDFA is utilized after the hub TX to boost the signals before being sent toward the leaf nodes (downstream).

Each leaf node uses an individual laser wavelength/frequency to transmit 100 Gb/s traffic over 4 DSCs towards the hub in the upstream direction. Thus, the hub receives a fully populated 16-DSC spectrum (see Fig. 12(a)). To guarantee tight sub-carrier spacing (here ~ 320 MHz) and to prevent collisions between neighboring sub-carriers coming from different leaf nodes, the laser frequency control scheme described in Section III-D is applied. Note, although the experiments are performed using individual fibers for up- and downstream, the control scheme

TABLE II
TRANSMISSION DISTANCE AND LEAF TRANSMITTER POWER FOR SETUP SHOWN IN FIG. 12(A)

	Leaf-1	Leaf-2	Leaf-3	Leaf-4
Transmission distance (km)	25	5	10	50
Leaf transmitter power (dBm)	-5.5	-8.7	-8.0	-2.0

can also be used for bi-directional single fiber links as described in [25].

The hub TX, broadcasts 16 DSCs towards all the leaf nodes in the downstream direction. Each leaf node uses its coherent channel selection capability to receive a subset of 4 DSCs (out of 16) and performs demodulation and decoding (see Fig. 12(b)).

Fig. 12(c) shows the received spectrum at the hub side, captured on a high-resolution optical spectrum analyzer. Note that the spectrum is continuous but was captured with particular leaf nodes turned on, one at a time to better highlight the signal source. It is worth noticing that the power of the 16 DSCs is flat because the different exhibited path losses have been pre-compensated via the leaf TX optical power control mechanism (no external optical amplifiers), mentioned at the end of Section III-F. Table II summarizes the transmitted optical power per leaf for this experiment.

Fig. 12(d) shows constellation diagrams received at the hub RX (separated by polarization and DSC). Each of the constellations is clear and reaches Q factors well above the FEC threshold, resulting in post-FEC error-free P2MP communication.

To demonstrate the tolerance to power transients and the ability to dynamically add and drop DSCs, the output power

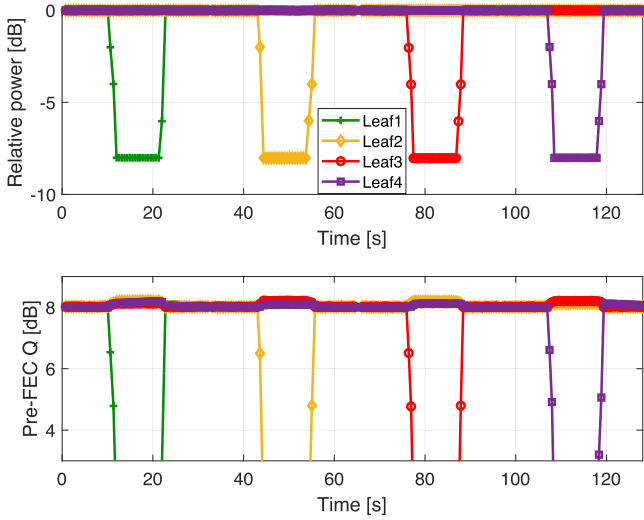


Fig. 13. (a) Relative power at VOA output; (b) pre-FEC Q-factor per leaf node on hub receiver.

of the DSCs of a 4 leaf nodes setup (similar to the one shown in Fig. 11(a) and (b)) was adjusted such that each leaf reaches a Q factor of 8 dB on the hub receiver. Transients are emulated by imposing a trapezoid attenuation profile (via external VOA) to the output of each leaf transmitter (one at a time).

Fig. 13(a) shows the attenuation profile vs. time. Each VOA changes its attenuation by 8 dB within ~ 1 s. Note the DSP processing can cope with much faster transients, but measurement speed and VOA control is limited. During the transition the Q factor performance of the affected DSCs follow the attenuation profile (Fig. 13(b)) and fall out-of-lock when the attenuation exceeds 5 to 6 dB due to the greatly reduced SNR. The DSC coming from the other leaf nodes are mostly unaffected during the transition (slight Q factor changes are visible due the changed noise conditions) and stay post-FEC error-free. This behavior proves the effectiveness of the gain control mechanism inside the RX DSP and the robustness to dynamic changes in channel counts.

V. CONCLUSION

Coherent optical systems, with their powerful DSPs, are widely used in metro, long haul, and intra-datacenter networks. Aggregation networks – at the edge of the core – may also use coherent pluggable modules for the link to the electrical aggregation site, but as of today, the transceivers connecting the customers are mostly direct detection.

Digital sub-carrier-based coherent transceivers provide a cost-effective solution to simplify the edge network architecture by removing the aggregation site and dramatically reducing the transceiver count. This is enabled by the DSP engine, which makes the point-to-multi-point operation possible.

The main building blocks of such a digital sub-carrier-based DSP are the same or very similar to well-known single-channel DSPs. However, there are several differences in detail. It is mostly the operation at lower symbol rates and intermediate

carriers that challenges the generation and demodulation of digital sub-carriers. On the other hand, the symbol rate reduces the complexity of the DSP especially for signal processing blocks counteracting link memory-related effects such as chromatic dispersion.

Digital sub-carrier requirements, as well as the special aspects of point-to-multi-point operation, have been discussed in this article. This analysis is supported by simulative results, as well as experiments measured on a real-time implementation of a 16 subcarrier 16QAM digital sub-carrier system with ~ 4 GBaud per sub-carrier, supporting a total capacity of up to 400 Gb/s. However, it is worth mentioning that the described aspects and principles apply to any digital sub-carrier implementation scheme regardless of the utilized modulation format and sub-carrier symbol rate.

APPENDIX A

TX IMPAIRMENTS IN FREQUENCY DOMAIN

The frequency domain representation of the drive signals into the optical modulator defined in Section III-E are

$$\begin{aligned} \mathcal{F}\{x_I(t)\} &= \underline{X}_{DSC,\Re}(\omega) * \frac{1}{2} (\delta(\omega + \omega_{DSC}) + \delta(\omega - \omega_{DSC})) \\ &\quad - i \cdot \underline{X}_{DSC,\Im}(\omega) * \frac{1}{2} (\delta(\omega + \omega_{DSC}) - \delta(\omega - \omega_{DSC})) \end{aligned} \quad (8)$$

$$\begin{aligned} \mathcal{F}\{x_Q(t)\} &= \underline{X}_{DSC,\Im}(\omega) * \frac{1}{2} (\delta(\omega + \omega_{DSC}) + \delta(\omega - \omega_{DSC})) \\ &\quad + i \cdot \underline{X}_{DSC,\Re}(\omega) * \frac{1}{2} (\delta(\omega + \omega_{DSC}) - \delta(\omega - \omega_{DSC})) \end{aligned} \quad (9)$$

with \mathcal{F} denoting the Fourier transformation, $*$ the convolution, and δ the Dirac impulse. $\underline{X}_{DSC,\Re}$ and $\underline{X}_{DSC,\Im}$ are the frequency domain representations of the real and imaginary components of the sub-carrier baseband signal

$$\underline{X}_{DSC,\Re}(\omega) = \mathcal{F}\{\Re\{\underline{x}_{DSC}(t)\}\} \quad (10)$$

$$\underline{X}_{DSC,\Im}(\omega) = \mathcal{F}\{\Im\{\underline{x}_{DSC}(t)\}\} \quad (11)$$

Solving the convolution in (8)–(9) yields

$$\begin{aligned} \mathcal{F}\{x_I(t)\} &= \frac{1}{2} (\underline{X}_{DSC,\Re}(\omega + \omega_{DSC}) + \underline{X}_{DSC,\Re}(\omega - \omega_{DSC})) \\ &\quad - i \cdot \frac{1}{2} (\underline{X}_{DSC,\Im}(\omega + \omega_{DSC}) - \underline{X}_{DSC,\Im}(\omega - \omega_{DSC})) \end{aligned} \quad (12)$$

$$\begin{aligned} \mathcal{F}\{x_Q(t)\} &= \frac{1}{2} (\underline{X}_{DSC,\Im}(\omega + \omega_{DSC}) + \underline{X}_{DSC,\Im}(\omega - \omega_{DSC})) \\ &\quad + i \cdot \frac{1}{2} (\underline{X}_{DSC,\Re}(\omega + \omega_{DSC}) - \underline{X}_{DSC,\Re}(\omega - \omega_{DSC})) \end{aligned} \quad (13)$$

Considering impairments defined in Section III-E, the output of the optical modulator in frequency domain becomes

$$X_{opt}(\omega) = A \cdot \mathcal{F}\{x_I(t)\} + iB \cdot \mathcal{F}\{x_Q(t)\}, \quad (14)$$

which expands to

$$\begin{aligned}
X_{opt}(\omega) = & + \frac{1}{2} \cdot \underline{A} \cdot (\underline{X}_{DSC,\Re}(\omega + \omega_{DSC}) \\
& + \underline{X}_{DSC,\Re}(\omega - \omega_{DSC})) \\
& - \frac{1}{2} \cdot \underline{B} \cdot (\underline{X}_{DSC,\Re}(\omega + \omega_{DSC}) \\
& - \underline{X}_{DSC,\Re}(\omega - \omega_{DSC})) \\
& - i \cdot \frac{1}{2} \cdot \underline{A} \cdot (\underline{X}_{DSC,\Im}(\omega + \omega_{DSC}) \\
& - \underline{X}_{DSC,\Im}(\omega - \omega_{DSC})) \\
& + i \cdot \frac{1}{2} \cdot \underline{B} \cdot (\underline{X}_{DSC,\Im}(\omega + \omega_{DSC}) \\
& + \underline{X}_{DSC,\Im}(\omega - \omega_{DSC})) \quad (15)
\end{aligned}$$

$$\text{with } \underline{A} = \sqrt{1 - \frac{IB-1}{IB+1}} e^{-i\omega\frac{\tau}{2}} e^{-i\frac{\theta}{2}}$$

$$\text{and } \underline{B} = \sqrt{1 + \frac{IB-1}{IB+1}} e^{+i\omega\frac{\tau}{2}} e^{+i\frac{\theta}{2}}$$

Without impairments that yield a sub-carrier at an intermediate frequency ω_{DSC}

$$\begin{aligned}
X_{opt}(\omega) = & \underline{X}_{DSC,\Re}(\omega - \omega_{DSC}) \\
& + i \underline{X}_{DSC,\Im}(\omega - \omega_{DSC}) \Big|_{\underline{A}=\underline{B}=1} \quad (16)
\end{aligned}$$

REFERENCES

- [1] D. Welch et al., "Digital subcarrier multiplexing: Enabling software-configurable optical networks," *J. Lightw. Technol.*, vol. 41, no. 4, pp. 1175–1191, Feb. 2023.
- [2] R. Bonk et al., "50G-PON: The first ITU-T higher-speed PON system," *IEEE Commun. Mag.*, vol. 60, no. 3, pp. 48–54, Mar. 2022.
- [3] X. Liu, "Evolution of fiber-optic transmission and networking toward the 5G era," *Iscience*, vol. 22, pp. 489–506, 2019.
- [4] J. S. Wey and J. Zhang, "Passive optical networks for 5G transport: Technology and standards," *J. Lightw. Technol.*, vol. 37, no. 12, pp. 2830–2837, Jun. 2019.
- [5] L. A. Campos, Z. Jia, H. Zhang, and M. Xu, "Coherent optics for access from P2P to P2MP," *IEEE J. Opt. Commun. Netw.*, vol. 15, no. 3, pp. A114–A123, Mar. 2023.
- [6] H. Sun et al., "800G DSP ASIC design using probabilistic shaping and digital sub-carrier multiplexing," *J. Lightw. Technol.*, vol. 38, no. 17, pp. 4744–4756, Sep. 2020.
- [7] M. Qiu et al., "Digital subcarrier multiplexing for fiber nonlinearity mitigation in coherent optical communication systems," *Opt. Exp.*, vol. 22, no. 15, pp. 18770–18777, 2014.
- [8] M. S. Neves, P. P. Monteiro, and F. P. Guiomar, "Chromatic dispersion-aware carrier-phase estimation for digital subcarrier multiplexing systems," in *Proc. Eur. Conf. Opt. Commun.*, 2020, pp. 1–4.
- [9] A. Napoli et al., "Enabling router bypass and saving cost using point-to-multipoint transceivers for traffic aggregation," in *Proc. Opt. Fiber Commun. Conf.*, 2022, paper W3F–5.
- [10] D. Welch et al., "Point-to-multipoint optical networks using coherent digital subcarriers," *J. Lightw. Technol.*, vol. 39, no. 16, pp. 5232–5247, Aug. 2021.
- [11] J. Hernández, F. Arpanaei, G. Martínez, Ó. G. D. Dios, J. Fernández-Palacios, and A. Napoli, "Clustering-based dynamic bandwidth allocation for point-to-multipoint coherent optics," in *Proc. IEEE Opt. Fiber Commun. Conf. Exhib.*, 2023, pp. 1–3.
- [12] J. Bäck et al., "A filterless design with point-to-multipoint transceivers for cost-effective and challenging metro/regional aggregation topologies," in *Proc. Int. Conf. Opt. Netw. Des. Model.*, 2022, pp. 1–6.
- [13] S. J. Savory, "Digital coherent optical receivers: Algorithms and subsystems," *IEEE J. Sel. Topics Quantum Electron.*, vol. 16, no. 5, pp. 1164–1179, Sep./Oct. 2010.
- [14] C. Fludger, T. Duthel, P. Hermann, and T. Kupfer, "Jitter tolerant clock recovery for coherent optical receivers," in *Proc. Opt. Fiber Commun. Conf.*, 2013, paper OTh1F–3.
- [15] X. Zhou and X. Chen, "Parallel implementation of all-digital timing recovery for high-speed and real-time optical coherent receivers," *Opt. Exp.*, vol. 19, no. 10, pp. 9282–9295, 2011.
- [16] B. Almeroth and G. Fettweis, "The impact of jitter on the signal-to-noise ratio in uniform bandpass sampling receivers," in *Proc. IEEE 79th Veh. Technol. Conf.*, 2014, pp. 1–5.
- [17] S. J. Savory, "Digital filters for coherent optical receivers," *Opt. Exp.*, vol. 16, no. 2, pp. 804–817, 2008.
- [18] T. Kupfer, A. Bisplinghof, T. Duthel, C. Fludger, and S. Langenbach, "Optimizing power consumption of a coherent DSP for metro and data center interconnects," in *Proc. Opt. Fiber Commun. Conf.*, 2017, paper Th3G–2.
- [19] I. Slim, A. Mezghani, L. G. Baltar, J. Qi, F. N. Hauske, and J. A. Nossek, "Delayed single-tap frequency-domain chromatic-dispersion compensation," *IEEE Photon. Technol. Lett.*, vol. 25, no. 2, pp. 167–170, Jan. 2013.
- [20] T. Pfau, S. Hoffmann, and R. Noe, "Hardware-efficient coherent digital receiver concept with feedforward carrier recovery for M -QAM constellations," *J. Lightw. Technol.*, vol. 27, no. 8, pp. 989–999, Apr. 2009.
- [21] R. Nagarajan, I. Lyubomirsky, and O. Agazzi, "Low power DSP-based transceivers for data center optical fiber communications (invited tutorial)," *J. Lightw. Technol.*, vol. 39, no. 16, pp. 5221–5231, Aug. 2021.
- [22] T. Pfau, "Carrier recovery algorithms and real-time DSP implementation for coherent receivers," in *Proc. OFC*, 2014, pp. 1–17.
- [23] I. Fatadin, D. Ives, and S. J. Savory, "Laser linewidth tolerance for 16-QAM coherent optical systems using QPSK partitioning," *IEEE Photon. Technol. Lett.*, vol. 22, no. 9, pp. 631–633, May 2010.
- [24] A. Kakkar et al., "Comprehensive study of equalization-enhanced phase noise in coherent optical systems," *J. Lightw. Technol.*, vol. 33, no. 23, pp. 4834–4841, Dec. 2015.
- [25] S. Ranzini et al., "Local and remote laser frequency control in point-to-multipoint networks using digital subcarriers," in *Proc. 49th Eur. Conf. Opt. Commun.*, 2023.
- [26] C. R. Fludger and T. Kupfer, "Transmitter impairment mitigation and monitoring for high baud-rate, high order modulation systems," in *Proc. ECOC 42nd Eur. Conf. Opt. Commun.*, 2016, pp. 1–3.
- [27] G. Bosco, S. M. Bilal, A. Nespola, P. Poggiolini, and F. Forghieri, "Impact of the transmitter IQ-skew in multi-subcarrier coherent optical systems," in *Proc. Opt. Fiber Commun. Conf.*, 2016, paper W4A–5.
- [28] L. Fan et al., "Hardware-efficient and robust DSP scheme for coherent DSCM system in presence of transmitter IQ impairments," *J. Lightw. Technol.*, vol. 41, no. 19, pp. 6187–6198, Oct. 2023.
- [29] A. Rashidinejad et al., "Real-time point-to-multipoint for coherent optical broadcast and aggregation-enabled by digital subcarrier multiplexing," in *Proc. Opt. Fiber Commun. Conf.*, 2023, paper W3H.1.